Metrol. Meas. Syst., Vol. 32 (2025), No. 3
DOI: 10.24425/mms.2025.155799

PAN POLSKA AKADEMIA NAUK

METROLOGY AND MEASUREMENT SYSTEMS
Index 330930, ISSN 0860-8229
www.metrology.wat.edu.pl

M&MS

INFLUENCE OF RADIATION SPECTRAL CHARACTERISTICS ON THE ACCURACY OF OPTICAL COHERENCE TOMOGRAPHY (OCT) USING A LASER-PLASMA SOURCE OF SOFT X-RAYS AND EXTREME ULTRAVIOLET

Antony Jose Arikkatt, Karol Adam Janulewicz, Andrzej Bartnik, Henryk Fiedorowicz, Przemysław Wachulak

Institute of Optoelectronics, Military University of Technology, Kaliskiego 2, 00-908 Warsaw, Poland (✉ *wachulak@gmail.com*)

Abstract

The paper presents an analysis of specific spectra manipulation and its metrological consequences for optical coherence tomography (OCT) in the nanometer wavelength range using a laser-plasma source of soft X-rays (SXR) and extreme ultraviolet (EUV). The focus is on extending the recorded spectra, predominantly through the stitching method. A model spectrum is used to validate the technique and transparently demonstrate the behavior of the stitched spectral components. The model is followed by processing the experimental data and demonstrating two possible destructive factors for data processing. The first factor is an unbalanced spectrum. While spectral extension toward higher photon energies significantly improves spatial resolution, it appears to be a second destructive factor. The presented results also highlighted certain technological and physical issues related to material properties of the sample, such as potential plasmonic effects. Consequently, the results, although offering much greater flexibility and ability to adjust the final spectrum, providing better reconstruction, also recommend caution in the scope and choice of the applied modification method.

Keywords: optical coherence tomography, X-ray coherence tomography, nanometer resolution, spectral modification, metrology, laser-plasma source, extreme ultraviolet, soft X-rays.

1. Introduction

Radiation spectra are exploited in many applications requiring different specifications and processing methods. Parameters such as spectrum bandwidth or spectral profile of intensity (the spectral power density) are of critical importance for these applications. In some of them, *e.g.* in *X-ray absorption spectroscopy* (XAS) [1, 2], the effect of linear combining (stitching) of spectra recorded in different (*e.g.* subsequent) measurements in adjacent spectral ranges while maintaining the same experimental arrangement [3] is easily to control and intuitively perceptible. The possible effects of interaction between matter and photons of higher energy are usually treated then as an inherent phenomenon. In fact, the method of scanning the beamline wavelength, typical for synchrotron sources, is a specific form of spectral stitching. In some applications, such as *X-ray coherence tomography* (XCT), the extraction of information hidden in the entire registered spectrum requires complex data post-processing, resulting in an *autocorrelation function* (ACF) that combines elements of the whole spectrum at each step [4-7]. XCT is understood here as a short-wavelength variant of the well-established *optical coherence tomography* (OCT), performed using radiation in the *soft X-rays* (SXR) / *extreme ultraviolet* (EUV) range [8-10] and some solutions of the OCT technique can be directly applied to it.

XCT, operating in the nanometer wavelength range, encompassing soft X-rays and extreme ultraviolet, has its own specific limitations, mainly experimental, as well as some

Article history: received July 29, 2025; revised August 5, 2025; accepted August 6, 2025; available online August 8, 2025.

complications. These include practically unavoidable filtering, due to high orders of diffraction, scattered visible and infrared radiation, and the often complex spectral structure of the source, especially when plasma-based sources are applied. Moreover, high-energy photons can modify the irradiated material to some extend by interacting with it, even if the flux is less than moderate. Effects include emitted secondary radiation, an increase in free electron concentration due to ionization, as well as interband transitions. This may modify the spectrum and propagation conditions, but has never been directly considered in the context of phase-sensitive measurements such as XCT. On the other hand, from a metrological perspective, short-wavelength radiation offers unprecedented axial resolution of the order of a few nanometers [5-7].

Using a laser plasma source of soft X-rays, a resolution of 2 nm has been demonstrated to enable information to be extracted from a multilayer reflecting structure [7], which is approximately three orders of magnitude better than the resolution of OCT, typically applying visible or near-infrared radiation [9]. This parameter depends primarily on the spectral bandwidth of the applied radiation [8, 10, 13], and linear combination of spectra may still be a tempting approach to extend the available spectral range or reduce the level of coherence, thus optimizing the resolution of the method. Moreover, the considered spectra manipulation can help to optimize the dynamic range of the detector signal in the entire available spectral window or to overcome the limited spectral range of the spectrometer. Mapping complex reflecting (scattering) structures buried in a material opaque to visible light but permeable to short-wavelength radiation will be a main goal of the XCT technique in its future development. The XCT technique, together with diffraction tomography [14] or *low-coherence speckle interferometry* (LCSI) [15], may certainly be of interest for nanoelectronics and nanophotonics as a noninvasive imaging method with nanometer resolution.

The XCT/OCT principle requires a low level of *longitudinal coherence* (l_c), *i.e.* a narrow range of constructive interference or, in other words, broadband radiation. The problem of preferred source characteristics for OCT has been discussed in detail in the literature [9, 12, 16]. A wide bandwidth has been determined as a prerequisite for increasing the final resolution of the method, while a Gaussian spectrum shape has always been considered the most preferred. The latter preference is a serious challenge in the short-wavelength spectral range with typically complex contributions from spectral lines, bands (transition arrays), and the presence of absorption edges. Many factors, such as noise, dispersion, or numerical windowing/filtering, limit the method's axial resolution, but the battle for a broad spectrum is the first step toward improving the resolution. To overcome, in some sense, the limitation of the requirement for a broad and Gaussian-type spectrum, rarely generated by modern compact short wavelength sources, spectrum-tailoring methods can be employed. These methods are based on stitching parts of the spectrum to gain an advantage in the subsequent reconstruction process. Spectral manipulation by the stitching method has been demonstrated in a *spectral domain - optical coherence tomography* (SD-OCT) operating with visible radiation [3].

In the present paper, we apply and discuss for the first time the spectral stitching method as a means practicable in XCT. The XCT technique offers the potential to be used as a metrology tool with nanometer resolution, however, the influence of spectral parameters on its accuracy is crucial from a metrology perspective. The two spectral components used in stitching were generated by differently filtered radiation source both in the experimental scheme and the corresponding model. The interest in the possible reasons of a specific behavior after stitching, its consequences for the accuracy and practicality of the procedure are in focus, especially since different filtering of the radiation source resulted in different results both in the experiment with the same sample and in the model. The analysis begins with a simple numerical model, followed by a standard processing approach applied to real experimental data collected with the use of a laser plasma SXR/EUV source. Here, we would like to emphasize that we do not consider

phase retrieval, which is often used as the final data processing step. This procedure with its arbitrariness in the choice of numerical routines, even if it improves the output quality, *e.g.* finesse of the feature of interest, is not necessary to show the effects of spectral manipulation, which is the focus of this paper.

2. Problem formulation

The essence of the proposed stitching technique principle relies on the following procedure. Having a broad emission spectrum $F(k)$ and being enforced to use a specific filter with a transmission curve $F_1(k)$ significantly limiting the useful or effective spectral width by introducing a low-transmission range, one will reduce the method's resolution. The concept of an effective bandwidth B_{eff} was introduced to estimate the resolution limits in such a case. Determined in practice as a spectral area encompassing 98% of the total power, it is frequently used in the case of recorded signals with significantly different amplitudes over a broad spectrum. The B_{eff} value is responsible in such cases for the spectrum resolution [17]. It is obvious, that even broad but containing some areas of low-level (close-to-zero) intensity spectra are destructive in this aspect, as then the B_{eff} is reduced and, as a consequence of the Nyquist criterion ($\Delta x < 1/2B_{eff}$) [17], the sampling interval in the space domain (Δx) can be prohibitively large. Addition of a complementary filter of high transmission $F_2(k)$ in this low-level range, seems to be a more practical and active step on the way towards improvement. These two filters, when jointly applied during the same measurement, would transmit a prohibitively narrow spectrum of the useful photon flux (Fig. 1a). However, one can stitch together their high-level (high-intensity) parts, *e.g.* at the spatial frequency k_s, where both signals are identical or at a very close level, and obtain a relatively strong signal over the full width of the considered spectrum. The procedure can, of course, be extended to stitching multiple-spectra, if needed, and hence improve the flexibility and applicability of the proposed method. We also used three numerical spectral window filters (see Fig. 1b) to select or promote in the analysis specific parts of the spectrum. The other goal of this action was the reduction of artifacts and "ghost" features to increase ACF's signal dynamics, especially with complex and noisy spectra obtained in an experiment.

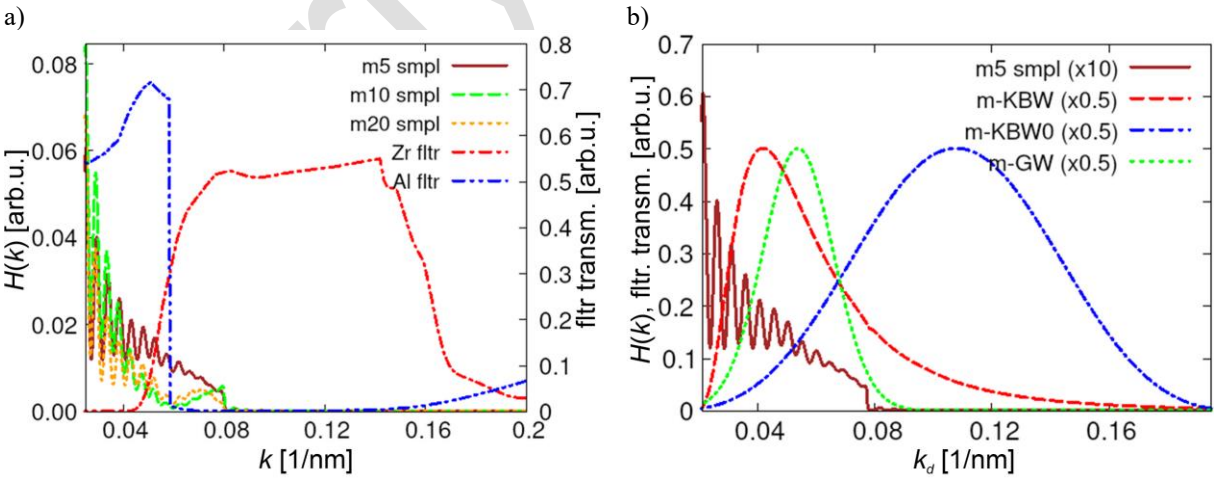

Fig. 1. a) The transfer functions (power reflectivity spectra) $H(k)$ of the modeled samples (*m5*-, *m10*- and *m20*-sample) together with the transmission curves of the applied source filters. b) The applied window filters on the background of *m5* sample 5 nm thick layer of Au-corrected.

Filters, also these numerical ones, can help in the spectrum modification. However, as they put a constraint on the spectrum widths, they will also reduce, to some extent, the available

resolution level. Generally, two types of the numerical window filters were used in the work and these were either of a *Gaussian window* (GW) or the *Kaiser-Bessel window* (KBW). All three applied window filters were distinguished by their shape and position. These used in modeling (*m-KBW*0, *m-KBW*, and *m-GW*) are presented in Fig. 1b together with the transfer function $H(k)$ of the sample. The number "0" was always used in connection with a window filter centered against the full available spectral range and covering it. The transform procedure with the use of a filter can be expressed as $\mathcal{F}^{-1}[H(k_d)\cdot G(k_d)] = h(z) \star g(z)$, where $G(k_d)$ is the window filter transmission in the dispersion-corrected spatial frequency domain. The right side of the expression is a convolution of the inversely transformed $H(k_d)$ and $G(k_d)$ in the space domain. Thus, the transform result of the window-filtered transfer function has to be deconvolved to be accurate.

In XCT (similarly to OCT in a non-interferometric or common-path configuration), the source signal reflected from the sample and normalized to a separately recorded reference signal constitutes the power reflectivity spectrum of interest, *i.e.* the functional dependence $S_{source}(k) / S_{ref}(k) = H(k)$ [6, 12, 13]. The resulting signal is formally the normalized reflected spectral power density and contains encoded information about the reflective structure (often multi-layer) buried below the host material's surface. In other words, it is a transfer function of the sample, typically denoted as $H(k)$ in the Fourier optics [17-19]. This "distributed" power reflectance is at first glance a function of the reflector position z and the incident radiation phase, *i.e.* the optical path length. Since the spectral power density in the spatial frequency domain is directly related to the ACF of the signal in the space domain by the *Wiener-Khinchine theorem* (WKT), more precisely by the *inverse Fourier transform* (IFT) $\mathcal{F}^{-1}[H(k)] = |r(z, \phi)|^2$, we took the dispersion-corrected ACF as a measure to estimate and compare the consequences of spectral modification. It is expected that ACF will be sufficiently narrow to undoubtedly identify sharp peaks (features) indicating the position of the hidden reflecting objects. Data acquisition and subsequent processing were performed (in all variants) by the same procedure to compare the results in a simple and reliable way.

3. Theoretical model

We designed a simple model consisting of a single Au film buried 100 nm beneath the surface of a silicon wafer to demonstrate some important effects of the spectral modification. The primary Au layer of the design had a thickness values of 5 nm (the sample denoted as *m5*) but we considered also two other gold layer thicknesses of 10 nm and 20 nm (the samples *m10* and *m20*, respectively). These variants of the sample were analyzed under spectrally uniform irradiation in two wavelength ranges: 5 – 40 nm, containing a low-level, close-to-zero and noisy part of a significant length, and 10 – 32 nm, a wavelength sub-domain with significantly reduced low-level component. The *m10*- and *m20*-samples were used to observe the effect of introducing two interfaces (Si/Au and Au/Si) separated by a distance larger than or at least equal to the shortest wavelength.

Parameters of the sample and irradiation were selected to match the conditions of the experiment described later. The transfer functions of such samples were taken from the CXRO database containing semi-empirical data [20]. The spectral dependencies of the $H(k)$ in the main pre-selected spectral range of 5 – 40 nm and for three different Au-layer thicknesses, are visible in Fig. 1a, together with the transmission curves of the applied source filters. These are represented by a Zr-film of 200 nm in thickness and a 250 nm thick Al film.

We decomposed the full wavelength range (5 - 40 nm) into two different regions with the dominance of one of two differently filtered photon fluxes in each. These regions met at $k_{sm} \approx 0.056$ nm^{-1} as shown in Fig. 1a. The source's filtering process was conducted directly on the sample's $H(k)$, and this was in our model fully equivalent to filtering the source.

A 100 nm-thick silicon layer above the Au film was the dominant, optically dense material of the sample. The radiation propagating in it is delayed relative to propagation in the free space. The propagating radiation was transferred, taking the CXRO dispersion data into account, to a new coordinate in the spatial frequency domain, and denoted it as k_d. This process is called dispersion correction. The functional relation between k_d and the wave number k_0 in the free space was calculated according to the principle given *e.g.* in [21].

After introducing the dispersion correction, and utilizing zero-padding to improve presentation resolution (sampling) of the results, we applied the IFT to determine the spatial position of the metallic structure buried in the silicon wafer (Fig. 2). Padding relies on adding a block of zeros to the data and increasing on this way a sampling rate for the transform without influencing the values of the processed vector. Execution of this step has confirmed one critical problem arising due to filter-caused shortening of the radiation effective bandwidth (green chained and brown dashed lines in Fig. 2a, *i.e.* weakening the signal amplitude and splitting the ACF peak for irradiation from a specific spectral range, represented here by the Zr-filtered component (dashed brown) or by the corresponding window filter position (*KBW0* – green). In other words, the same sample (*m5*) gives different results depending on the spectral composition of the applied irradiation.

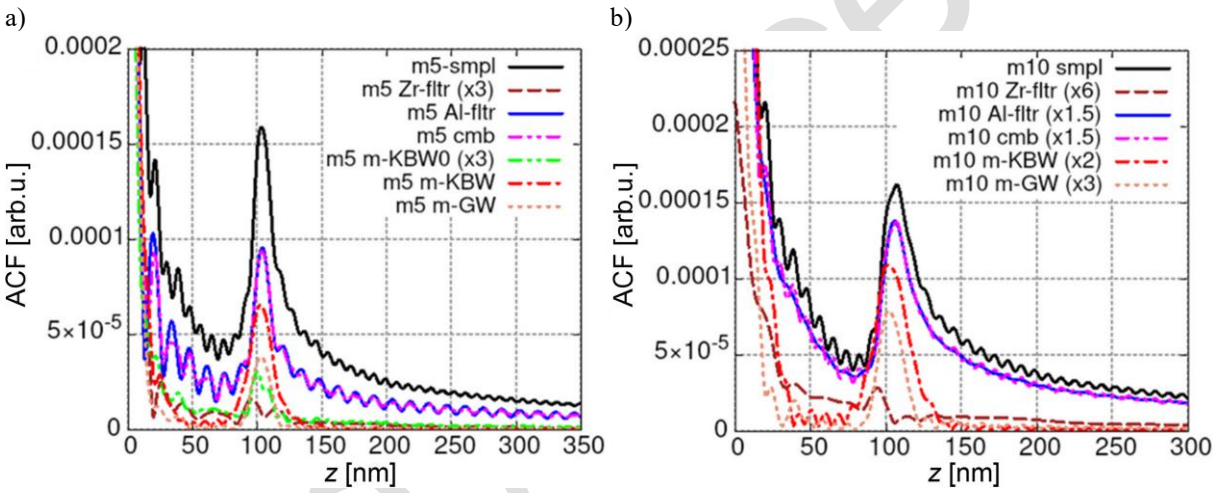

Fig. 2. a) The *ACF*s from modeling the *m5*-sample irradiated at a uniform level (CXRO-data without windowing) compared with the ACFs resulting from irradiation by the Zr-filtered and Al-filtered radiation source; combined spectrum (*cmb*) includes the parts from Zr- (weak) and Al-filtered (strong) source radiation stitched at k_{sm}; the window filtering of the *m5*-sample was realized by the *m-GW*, *m-KBW*, and *m-KBW0* filters. Please, turn attention to the equality between the results of the Al-filtered radiation (blue solid line) and the combined spectrum *m5 cmb* (magenta dash-dotted line) as the curves nearly perfectly overlap each other. The curves were multiplied by the factors listed in the legend to present the results more transparently. b) The ACFs obtained with the *m10*-sample (10 nm thick Au film). The applied spectral range was in both cases between 5 and 40 nm. Colors are identical to improve the readability and the possible comparison.

3.1. Spectral range

We applied two different spectral ranges in the model calculations. The narrower one (10 – 32 nm) offered the sample's transfer function with a very short part at a level close to zero (equivalent to a broad B_{eff}), while the other one (5 – 40 nm) of the same B_{eff} value had significantly wider total width and contained more energetic spectral components even if at significantly lower intensity level.

3.1.1. Spectral range 5 – 40 nm

The modeling results in the spectral range 5 – 40 nm are shown in Fig. 2a in the form of ACFs. The result of windowing implies one interesting effect. The peak of interest of all filters

is towards lower *z,* and even more, the *m*-sample filtered with the *m-KBW0* (the green chained line in Fig. 2a tends to behave similarly to the Zr-filtered component (two peaks within the brown dashed trace). Both are split into two parts and the stronger peak is shifted towards lower *z* even more than those obtained with other filters. We looked after the correlation between the shapes and positions of both transformed spectra. This observation suggests that a spectral composition with dominance of shorter wavelengths (higher *k*) is responsible for such a measurement output. The same conclusion is valid also for the plots in Fig. 2b.

We do not think that deconvolution is necessary in the space domain to compare the results, and will not reverse the peak splitting. So, at this point, one cannot doubtlessly conclude that the relation between the high- and low-level signal parts is the only reason responsible for the effect. The IFT output in the form of brown dashed ACF line labeled as *m5* Zr-filter in Fig. 2a does not deliver in this case any unambiguously recognizable feature related to the buried Au layer and the ACF is split into two "lobes" shifted in opposite directions from the nominal value of 100 nm. Thus, a broad but dominantly low-level signal does not guarantee any reasonable identification of the buried structure. As the behavior of the stitched spectra under such idealized conditions was a very important aspect for our interest, we merged the Zr- and Al-filtered $H(k)$ spectra at $k_{sm} = 0.056$ nm^{-1}, the crossing-point of both spectra . Stitching of both components can be treated as a sort of a non-zero appendage to the Al-filtered transfer function to extend the spectral region or conversely, an addition of a strong Al-filtered signal to the relatively weak and narrow Zr-filtered transfer function to improve the general spectrum quality. The stitched spectrum is dominated by its high-intensity part originating from the Al-filtered radiation, and it is no surprise that the IFT results of such a combined (stitched) signal nearly perfectly overlap that of the transformed Al-filtered ones (see Fig. 2a and Fig. 2b).

As far as the larger thickness of the Au layer are concerned (*m10*), the results show some substantial changes. The Zr-filtered radiation gave a typical very weak peak split after the transform and shifted far from the nominal depth value. The 10 nm-thick Au layer delivers, after irradiation by the Al-filtered radiation, a single, reasonably pronounced peak of the feature but slightly deviated from the nominal value towards a larger depth (see Table 1 and Fig. 2b). The shape of the peak suggests that we could see two reflections subject to better resolution. The second of these peaks would be in the position of the curve's strong roll-off on the leading edge, *i.e.* a few nanometers earlier.

Table 1. Modeling results of *m*-sample - a depth of the Au foil in [nm]; two different spectral ranges of irradiation and metal layers of different thicknesses are considered.

Case	**Sample**	**Spectral range**	
		5 - 40 nm	**10 - 32 nm**
No filtering	*m5*-sample	103.6±0.5	100.1±1.2
	m10-sample	107.4±0.5	97.7±1.2
Zr filtering	*m5*-sample	95.4±0.5 115.0±0.5	96.5±1.2 114.3±1.2
	m10-sample	94.4±0.5	94.1±1.2
Al filtering	*m5*-sample	103.6±0.5	100.1±1.2
	m10-sample	106.0±0.5	98.9±1.2
Combined spectra	*m5*-sample *cmb1*	103.6±0.5	100.1±1.2
	m10-sample *cmb1*	106.9±0.5	-

In the case of combined or stitched spectra, the weak and narrower spectrum (Zr-filtered) is in such a combination (here with Al-filtered radiation) fully dominated by the appended spectrum of a high spectral density; its ACF is nearly identical to that of the spectrum's stronger

part. While the curves drawn with the purple (*cmb*) and blue (Al-filtered) lines in Fig. 2a and Fig. 2b overlap each other in the full range, and the position values are also nearly identical (Table 1). The IFT of the combined signal is stronger, showing the feature of interest at a reasonable level and proving the advantage of spectral stitching and manipulation. The multiplication (scale) factors were also used here to clearly present all curves. Moreover, the extracted peak positions (positions of the buried Au layer), excluding that for pure Zr-filtering, are nearly identical and even much closer to the nominal value of 100 nm. This confirms the assumption that stitching the spectra can be a method or remedy for improvement of the output signal, subject to the stitched (appended) signal being strong and broad. The improvement is evident, and the result is accurate.

3.1.2. Spectral range 10 – 32 nm

For the sake of comparison and stressing the role of the radiation bandwidth, the results of irradiation in a much narrower spectral range (10 – 32 nm), with an energy bandwidth of about 85 eV, approximately 2.5 times narrower than that in the previous case, are shown in Fig. 3a. It is clearly visible that all peaks are shifted towards lower *z*, while the exclusive filtering with Zr-filter (yellow chained line) splits the peak. All the extracted from the model positions of the gold layer buried in silicon are collected in Table 1.

Slightly more than a half of this spectral range is covered by the *m*-sample's transfer function at a noticeable level (Al-filtered) but it also includes the whole Zr-filtered component combined with a near-zero component of a comparable length (see inset to Fig. 3a). Interestingly, the presence of peak split in this case also suggests that other than the low-level signal contribution is responsible for the effect, as the low-level components are noticeably narrower than those in the full-range (5 – 40 nm) spectrum and should therefore be less influential. However, a low-level signal, here the transfer function of the Zr-filtered radiation, when stitched with a strong and spectrally sufficiently broad signal, offers a reasonable identification of the Au layer position (*m5-cmb* trace in Fig. 3 and Table 1).

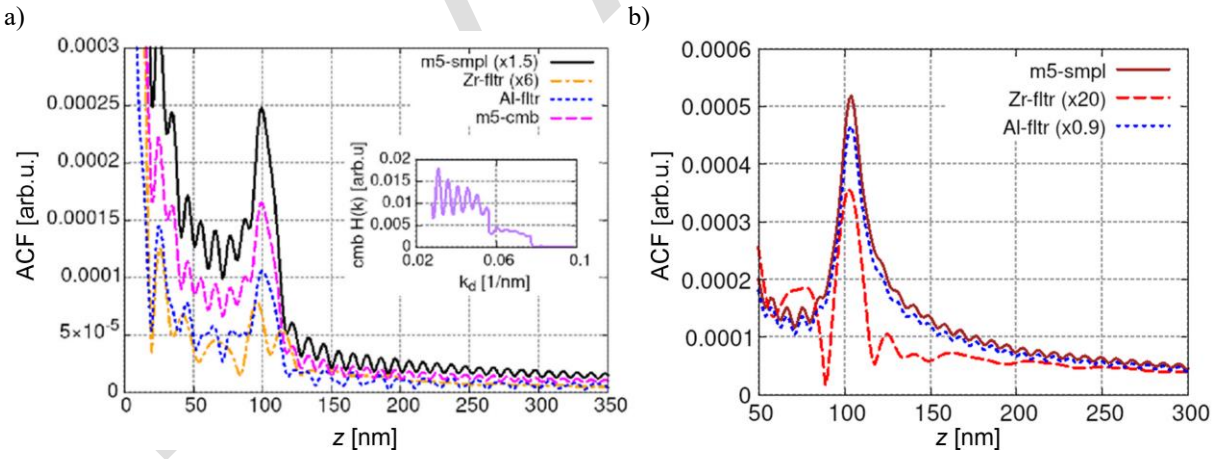

Fig. 3. a) The ACFs derived from the model for 5 nm Au foil and irradiated in the spectral range between 10 and 32 nm. The inset shows the combined $H(k_d)$ containing the Al- and Zr-filtered (the right-side of k_{sm} = 0.056 nm^{-1}) parts of the spectrum. b) The ACFs of the samples irradiated by differently filtered radiation but in the spectral range 12.8 nm – 40 nm.

3.2. The presence of gold layer

The spectral dependence of the results indicated critical influence of the shorter wavelengths (more energetic photons) on the results, mostly with the disturbing effect. This observation turned our attention to a quite specific aspect never considered in detail in the XCT or very rarely in the short-wavelength context. It is mostly about metal (most frequently Ag, Au)

surrounded by a low-loss semiconductor (Si) that here can be treated as a dielectric. This is a classical plasmonic environment, *i.e.* the situation of wave propagation in the structures of dimension smaller or comparable to λ. The considered ranges of wavelengths between 5 nm (248 eV) and 40 nm (31 eV) as well as between 10 nm (124 eV) – 32 nm (39 eV) match the pre-conditions reasonably well. Reflection in the classical optics is discussed at media interfaces. However, here the situation becomes slightly specific as we use irradiation of angular frequencies between 4.71×10^{16} rad/s (λ = 40 nm) and 3.77×10^{17} rad/s (λ = 5 nm) while the plasma angular frequency of Au $\omega_{pe} \approx 1.4\times10^{16}$ rad/s and that of silicon is even smaller and strongly dependent on free electron concentration. Thus, frequency of the probing radiation exceeds the host material's plasma (free electron gas) frequency in the whole applied spectral range. That leads to significant complications as such a plasma when irradiated at $\omega > \omega_{pe}$ used to generate plasmons, the quanta of the surface and bulk plasma oscillations, responsible for the reflection characteristics. Generation of the EUV plasmons was excellently and in a more general aspect addressed for the spectral range from 107 nm to 310 nm and was supported by experimental data for silicon [22]. In our XCT experiment we applied much shorter wavelengths but the quoted work suggests that the plasmonic effects are absolutely plausible.

As interaction of the applied energetic radiation with the bound electrons of the traversed material is possible, it can lead either to generation of new free electrons or promote the bound ones to a different state. In the case of gold, the binding energies of the electrons from the bands *O3* down to *N6* are in the range 57.2 - 87.6 eV [23], *i.e.* they are much lower than the highest energy of the available photons. Similar situation is for Si, where the highest binding energy of the shell *L* (*L1-L3*) corresponds to the range of 99.2 - 149.7 eV and that of *M* is between 8 eV and 2 eV (*M1-M3*).

It is worth stressing that direct interband transitions are not allowed in Si and these indirect are inefficient, especially in the short-wavelength range. This leads to an abundance of unbound electrons in the valence band [24]. Importantly, photons from the applied spectral range are able to remove some of the bound electrons, and the following process of filling the created vacancies could be a source of radiation acting as a sort of strengthened and spectrally localized noise. Silicon shows fluorescence at wavelengths between 91.2 eV (13.6 nm) and 147.7 eV (8.4 nm) caused by four different *L-M* transitions. There are also many possibilities of transitions from the noticeable density of occupied states in Au located slightly below the Fermi level [25].

Broad spectral range of the applied radiation and the presence of Au/Si interface including a depletion layer strongly influence the free-electron behavior [24]. Moreover, noticeable density of states close to the Fermi level of both elements as well as strong dependence of the silicon properties on the carrier concentration contribute markedly to the picture's complexity. One of the critical points seems to be the presence of the Si/Au and Au/Si interfaces. This diffuse, alloyed object was frequently analyzed and it was found that its irradiation causes the energy states *5d* in gold and *2p* with *4f* in silicon undergo some splitting or shift in silicon [26, 27]. Additionally, such a structure offers when irradiated a rich spectrum of the Auger electrons [28] and all of this happens especially in the spectral range between 90 eV (13.8 nm) and 100 eV (12.4 nm). That creates a complex picture of the material electronic structure and resulting secondary emission. For this reason more detailed analysis of the effects in the context of XCT requires a comprehensive and challenging work and is out of scope of this paper. The modelling results suggest that Au is the key player in the whole process. The evidence of that seems to be supported by the plots of $H(k)$ and $dH(k)/dk$ in Fig. 4. First of all, the period of the oscillations evidently changes with k. These changes are better visible in Fig. 4b where the derivatives of the transfer functions are plotted as a function of the spatial frequency. The crossing points of the derivative traces with the abscissa mark the extrema's positions of $H(k)$ and these depend on a thickness of the Au layer. Irregular changes in the k domain are observed

especially in the vicinity of the Si-absorption edge, roughly in the spectral range between 74.2 eV (16.7 nm or 0.06 nm^{-1}) and 105 eV (11.8 nm or 0.084 nm^{-1}) (see Fig. 4) and that is exactly the spectral range strongly influenced by the presence of the Au/Si interface. We limited here the k-domain range to the values between 0.055 and 0.09 nm^{-1} to make the discussed features visually more distinctive. The spectral region of a strong $H(k)$ deformation corresponds quite well to the reported emission of gold and silicon [29]. It is clearly seen that the retrieved $H(k)$ signal in the vicinity of $k \approx 0.06$ nm^{-1} (74.2 eV) is, for the samples $m10$ and $m20$, significantly reduced in comparison to the $H(k)$ of $m5$. While the thicker Au layers offer higher concentration of the interaction centers. This suggests an enhanced absorption occurring in this spectral range. Interestingly, all three traces are overlapped by similar oscillations, but as a whole they differ noticeably. The 10 nm-thick (*m10*) layer steepens the absorption edge of Si at 12.4 nm (100 eV and 0.08 nm^{-1}) while thicker variant of the foil (*m20*) with the local maximum at $k \approx 0.072$ nm^{-1} (89.3 eV) strongly limits and smears the edge. On the other hand, the gold layer of the same thickness but irradiated by differently filtered radiation does not change the oscillation frequency (Fig. 4c).

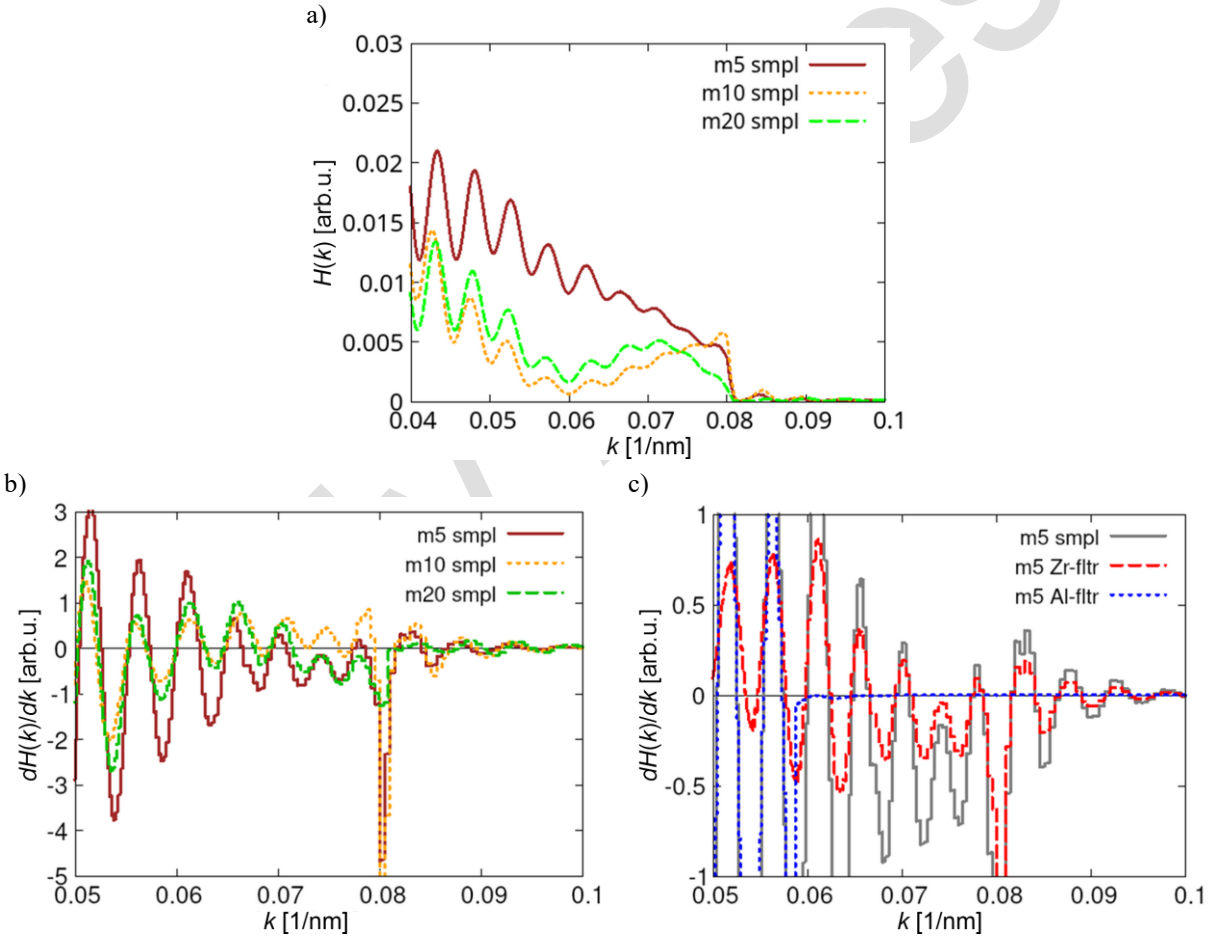

Fig. 4. a) The transfer functions for different thicknesses of the buried Au layer (5 nm, 10 nm, 20 nm) as a function of the spatial frequency. b) $dH(k)/dk$ as a function of the spatial frequency for three different thicknesses of the gold layer buried in a Si wafer. c) $dH(k)/dk$ as a function of the spatial frequency for the *m5* sample, but differently filtered source radiation. The sudden drop corresponds to the absorption edge of Si.

The observed correlation in these effects allows us to claim that the presence of the Au foil contributes to the effect. However, more careful inspection suggests that rather physical processes in the spectral range surrounding the Si L-absorption edge are responsible for that, and generally, a single-peak ACF for the Zr-filtered radiation is available already when the applied wavelengths exceed 12.8 nm (96.9 eV or 0.078 nm^{-1}) (Fig. 3b).

Here, we would like to point out to the changes in the ACF peak position when gold films of different thickness were used in our model. Two spectral windows *m-GW* and *m-KBW* eliminating or strongly limiting the contribution of high-frequency region reduce the depth value extracted from the full range data. One can conclude that the radiation component of higher-frequency (shorter-wavelength) strongly influences the output towards higher depth and this is consistent with the Drude model of the metal free-electron sea [24]. This brings us back to the discrepancy in the extracted Au-layer position when irradiated by differently filtered (Zr, Al) radiation. In both variants radiation propagates under strongly different conditions. Again, any detailed analysis of this aspect is out of the scope of this paper, but we want to point out some critical aspects of a new, plausible scenario.

Importantly, in all samples the Au layers are of different thicknesses, but were located at the same depth of 100 nm. That gives the supporting argument that the observed spectrum imperfection close to the absorption edge is strongly connected with the presence of the buried gold films. How critical can be the spectral position and shape of the transfer function is indicated by comparison of the plots in Fig. 5a and Fig. 5b. The first figure includes the transfer function obtained from Zr-filtered source together with three variants being the results of additional applying the numerical window filters (*m-KBW0*, *m-KBW* and *m-GW*) of shapes illustrated in Fig. 1b. These transfer functions after transform to the ACFs are presented in Fig. 5b. Surprisingly, the $H(k)$ obtained with the *m-GW* window does not give the split into two peaks, typical for the Zr-filtered radiation. Moreover, even if comparison of the transfer functions obtained with *m-GW* (orange dashed line) and *m-KBW* (green dashed) show minimal differences, the ACFs resulting from both differ markedly (Fig. 5b). The center of the under-curve-area's shifted towards lower spatial frequencies gives a single-peaked ACF, here accidently, at the nominal value of the Au layer depth. Noticeably, the transfer function with the use of the *m-KBW* window (green dashed line) is only slightly weaker at the peak than that with the *m-GW* but has minimally higher level at the edge position (under-curve-area's center shifted towards higher k_s). This is sufficient to observe the initial phase of the typical ACF split (green dashed line in Fig. 5b) absent in the case of *GW* filtering. This speaks for the conclusion that the $H(k)$ level at the *L*-absorption edge of Si (12.4 nm) decides about the ACF structure.

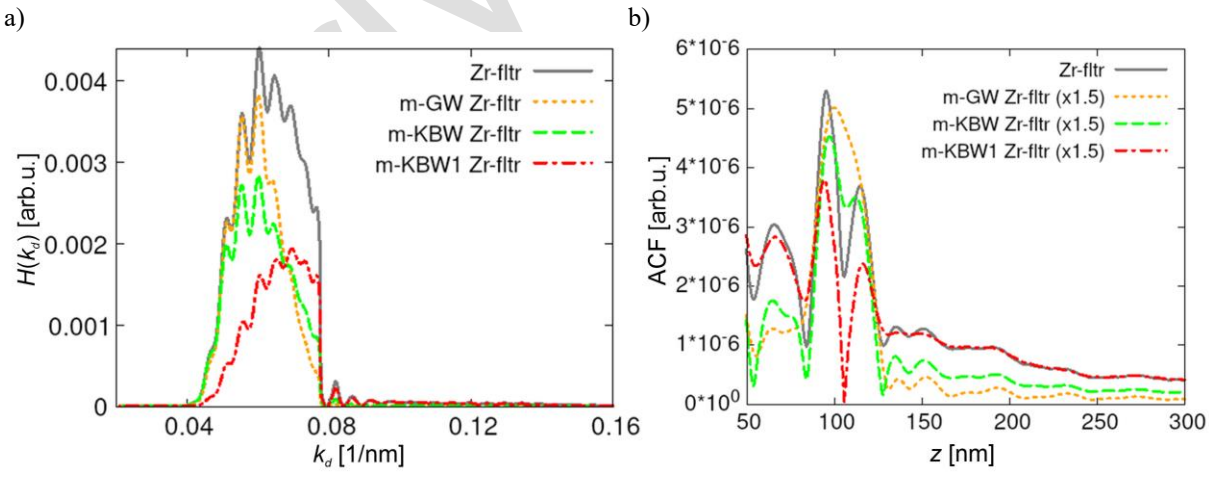

Fig. 5. a) Transfer functions $H(k)$ of the Zr-filtered source radiation without any additional numerical filtering (solid line) and modified by three different window filters presented as a function of the spatial frequency. b) ACFs of the transfer functions presented within the panel a).

We also found that the single ACF peak demands the $H(k)$ positioned above 12.8 nm (96.9 eV or 0.078 nm^{-1}) as it was shown in Fig. 3b. Reduction in the contribution of the more energetic radiation gradually eliminates the ACF split destroying the measurement (two values given in Table 1). The comparable widths of the $H(k)$s in Fig. 5a suggest that this is not the

resolution problem. A relatively strong signal and the low-k end of the $H(k)$ reduce to some extend the absorption edge areas' influence. This can be retrieved from the results plotted with the solid and chained lines in Fig. 5a and Fig. 5b.

3.3. Conclusions from the model

The model calculations suggest that the spectral composition of the processed signal can have a destructive influence on the measurement output. Wide, low-level parts seem to act as a sort of non-zero-padding, but with negative consequences, especially if they have a character of noise. The destructive influence appeared in modeling, even with the smooth low-level signals. Padding, being a linear interpolation process, quite well reproduces the peak positions and can "repair" the output when the transformed signal shows a limited sampling rate. The spectrum parts of high-level intensity should dominate in the processed spectra but this should be well balanced as a whole as it was shown in the example of window filtering with *m-KBW* and *m-GW* (see Fig. 2b and Fig. 3a). All model calculations, were relatively precise and accurate, especially in the case of the narrower spectrum (10 – 32 nm) and this claim is supported by the presented data. The use of the broader spectrum (5 – 40 nm) to increase resolution, even if it contains the low-intensity part extended within two-thirds of the whole spectrum width, gave the results more deviated from the nominal value of 100 nm. Taking into account our experimental conditions, the assumed spectral bandwidth was quite wide ($2B$ = 35 nm, corresponds to 217 eV) and caused quite reasonable resolution but also still a noticeable line/feature broadening. *The Full Width Half Maximum* (FWHMs) of the extracted lines/features were about 17 nm and increased to 21 – 23 nm FWHM when windowed. The combined spectrum was stitched preferably at k_{sm} = 0.056 nm^{-1} with the high-end k_d values taken from the Zr-filtered signal and the part below k_{sm} belonged to the Al-filtered spectrum. The data processing produced the ACF peak determining the Au-layer position at 103.6 nm. This result should not be a surprise as the combined signal was fully dominated by the Al-filtered component giving the position at 104 nm. The small difference was very likely caused by the presence of the Zr-filtered component and this is well correlated to the results for the "unwindowed" sample.

The modelling also turned our attention to the physical process potentially occurring when photons of relatively high energy are used in the irradiation process. Processes as ionization, excitation, secondary emission, or even free electrons flow through the Si/Au interface, and plasmonic effects can influence the propagation (including reflection) conditions of the recorded radiation. The presented results also allow for the conclusion that the absorption edge itself is not responsible for the destroying effect as the Al absorption edge at 17.2 nm (0.058 nm^{-1}) does not cause an equal effect (see results in Fig. 3a).

4. Analysis of the experimental data

4.1. Experimental setup

Experimental data were collected during an XCT experiment conducted with a laser-plasma EUV source in the scheme presented in Fig. 6a. The collected data should be sufficient to verify our expectations regarding the undertaken spectral modifications. A 5 nm thick gold film was buried nominally 100 nm below the silicon wafer surface, and we denoted this sample as an *e*-sample (experimental sample) to easily distinguish the results from those obtained by modelling. The radiation emitted by the EUV source was recorded in the spectral range from 5 nm to 40 nm. The source radiation, filtered by Zr (200 nm thick) or Al (250 nm thick) films,

was focused onto the sample and, after reflection, directed through collecting optics to an EUV spectrometer consisting of an diffraction grating and a CCD sensor.

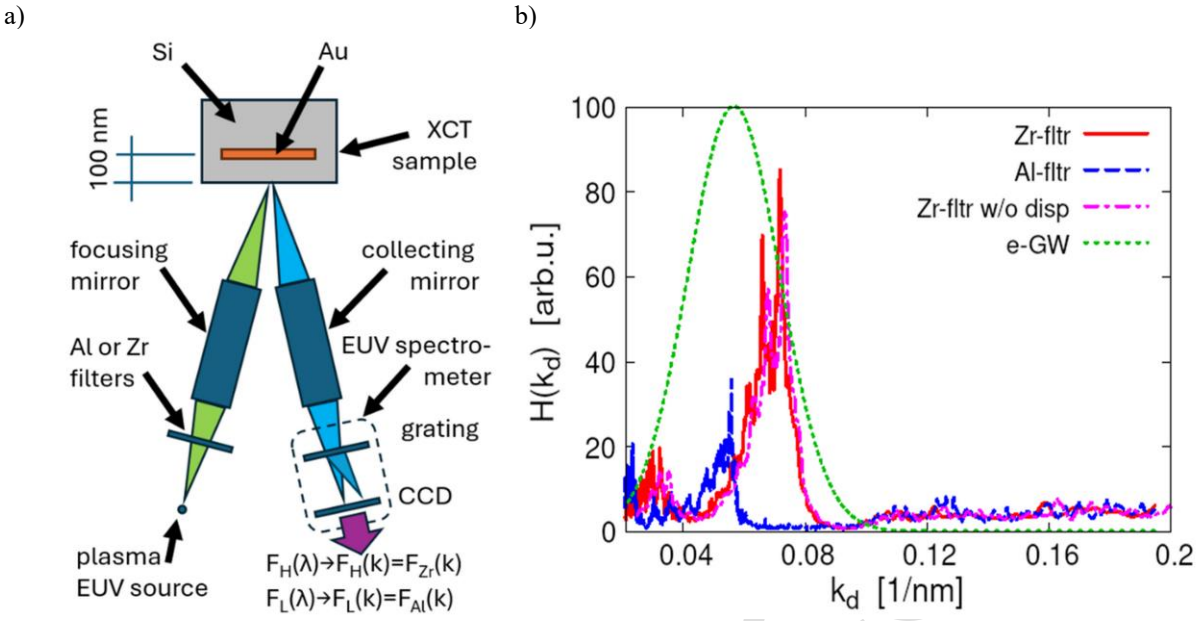

Fig. 6. a) The experimental setup applied in the investigation of the e-sample. b) The transfer functions retrieved in the experiment. Note that the chained orange line denoted in the legend as "Zr-filter w/o disp" corresponds to the values from the k_0 domain and demonstrates the scale of the dispersion effect (peak shift); the latter was added for the sake of completeness.

The transfer functions $F_{Zr}(k)$ and $F_{Al}(k)$ of the sample irradiated by a source with different filtering were retrieved from the signals recorded after reflection from the sample and normalized and shown in Fig. 6b. Of course, the geometry and parameters of the illumination and EUV radiation collection system, as well as the geometry and parameters of the EUV spectrometer, affect the spectra recorded during the experiment. All these parameters were taken into account in the signal processing according to the procedures described in detail in [29]. Using the standard normalization method, *i.e.*, dividing the signal reflected from the embedded structure by the signal reflected from the bulk silicon, we obtained the *e*-sample transfer function $H(k)$ presented together with the dispersion correction scale and the Gaussian window filter (*e-GW*) in Fig. 6b.

4.2. Results and analysis

The transfer functions, despite smoothing, were relatively noisy, and to avoid loss of information through excessive smoothing, we decided to apply the *e-GW* window filter (equivalent to *m-GW,* see Fig. 1b) to improve the quality of the transformation results. The obtained ACFs for the spectral range of 5 – 40 nm are shown in Fig. 7a. Those obtained for the spectral range of 10 – 32 nm are shown in Fig.7b. For a narrower bandwidth, we applied the *e-GW1* window filter with a shape similar to the *e-GW*, but shifted towards a smaller k by 0.002 nm^{-1}.

The combined $H(k_d)$ plot is a combination of the parts of the transfer functions shown in Fig. 6b, stitched at a k_d of ≈ 0.056 nm^{-1}. The ACF traces shown in Fig. 7 summarize the positions obtained in the experiment with the differently filtered signals and their specific combinations *e-cmb1* and *e-cmb2*. They were arranged in the same way as those in the model. The peaks associated with the position of the embedded Au film in the sample and the complete experimental output are summarized in Table 2. We found that the results obtained with

window filters can differ from those obtained without such filtering. The reason for that is that the resolution is reduced, and some closely located spikes are often "merged" in the filtered version in a weighted way. Both versions of the results are presented in Table 2.

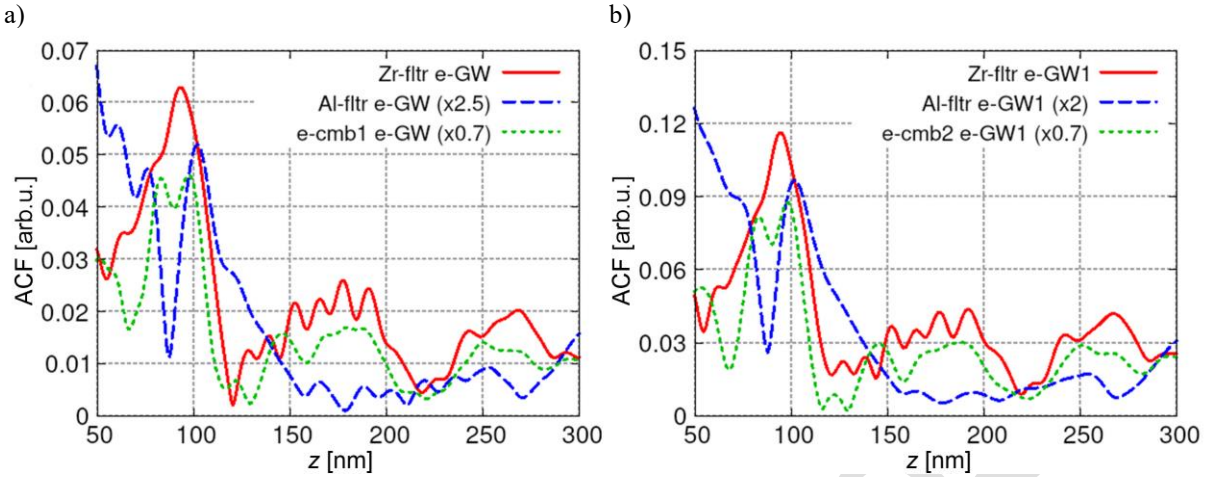

Fig. 7. a) The ACFs calculated from the filtered and combined (stitched *e-cmb1*) experimental data within the spectral range (5 – 40 nm) with application of the Gaussian window filter *e-GW*. b) the *ACF*s obtained for Zr- and Al-filtered radiation within the spectral range between 10 and 32 nm, together with the combined transfer function *e-cmb*2; all autocorrelation functions are obtained from the corresponding transfer functions modified with *e-GW*.

Table 2. Experimental results - depth of the A*u* foil in [nm]; here, *e-GW1* is a specific symmetric Gauss window shown in Fig. 6a.

Spectral range	Sample, filter	no window	e-GW or e-GW1
5 - 40 nm	e-sample Zr-fltr	93.5	98.3
	e-sample Al-fltr	102.1	101.6
	e-sample cmb-1	97.8	98.3
10 - 32 nm	e-sample Zr-filter	94,1	94.1
	e-sample Al-filter	102.4	100.1
	e-sample cmb-2	98.9	97.7

The *e-GW* filter (see its shape and position in Fig. 6b) extracts signals containing an almost dominant strongest component without a broad, low-level noisy part. The resulting ACFs presented in Fig. 7a clearly demonstrate the consequences of the shape of the spectral power density far from the "ideal case" used in the modelling. The "windowed" output is, as expected, broadened (20 nm for the Al-filter and 48 nm for the Zr-filter case) and tends to deviate strongly from the results referring to the original spectrum only for the wide applied spectrum (in this case 5 – 40 nm). This is due to the more peaked spectral structure resulting from the higher resolution. We applied another Gaussian window (*e-GW1*) centered within the high-level part of the transfer function at $k_d = 0.055$ nm^{-1}, limited to the spectral range from 10 to 32 nm.

In practice, the usual lack of knowledge of the nominal position of the buried reflector complicates the problem, and identifying the correct feature indicating the desired position can be difficult. The presented results do not recommend the use of widow filters in this process, and if so, it should be with reduced bandwidth or high spectral quality.

4.2.1. Spectral stitching

We applied the stitching technique to modify the recorded transfer function's $H(k_d)$ spectral composition in a similar way to that presented during modelling. While staying within the full width of the spectrum (5 – 40 nm) due to the resolution level, the modification was conducted

by determining k_{s1} (placed at 0.0564 nm^{-1}) as a stitching point where the part of the *Zr*-filtered spectrum lying above k_{s1} was stitched together with the Al-filtered $H(k_d)$ located below this point. This variant has been denoted as e-*cmb1*. Here, the high level of the Zr-filtered radiation replaced the corresponding weaker part belonging to the Al-filtered radiation. The sample denoted as *cmb2* was designed in the same way, with the same stitching point, but the components were of different widths due to the narrower spectral range. The combined transfer functions can be virtually identified in Fig. 6b. We also transformed the transfer function within the wavelength range above 12.8 nm. The result for the Zr-filtered radiation is very similar but shows essentially a single peak, even if its shape and width suggest that the additional one can be merged but not resolved.

The consequences of applying the stitching method in this way are visible both in Fig. 7 and Table 2. The extracted *ACF*s (dotted green traces - e-*cmb1* and e-c*mb2*) reasonably reproduce in all cases the results obtained from the uncombined spectra, even if the stitched spectrum shows a second peak resulting from the stronger dominating component (red solid). We also see that window filtering broadens strongly and hides some features, *e.g.* converts multi-peak composition into a single peak.

The transformed combined spectra delivered a quite consistent picture, but the quality of the features of interest was not always of the highest probe, mainly due to the character of the processed spectra (a significant spectral range with a very low and noisy signal in the original transfer function). There was an observable broadening effect originating from the reduced B_{eff}, and this is well seen if one compares Fig. 7a and Fig. 7b. Analysis of the obtained results allows us to conclude that the stitching procedure should be conducted very carefully, even if it works in a very predictable way in modelling. The claim that a weighted combination, *i.e.* comparable intensity and in some cases length of the merged/stitched spectral components would be beneficial, seems to be justified. Both, too short and two weak components, combined with the main part of the spectrum, introduce destructive factors for the following retrieval of the structure. The extracted ACFs were in such cases broader and, most importantly, noticeably shifted from the expected nominal position.

5. Summary and final conclusions

In this work, we verified the tempting possibility of combining well-pronounced parts of the spectra registered with the same experimental setup in neighboring spectral regions. It was performed to test the accuracy of the XCT reconstruction from the metrological point of view. Such approach would provide much greater flexibility and reduce the requirements for the applied recording apparatus. The possibility of simple spectrum manipulation and its consequences for the quality of the XCT/OCT measurement, as well as the influence of the optical properties of the sample's dominant material, were analyzed based on a simple theoretical model and a real experiment conducted with a laser plasma EUV source. The manipulation of the spectral components seems to be quite critical. Only spectral appendages of matched power density seem to be employed without negative consequences. As a result, spectra stitching as a method of the output amendment seems to work reasonably well, but requires caution in the choice of spectral components to be stitched. Finally, we have proven that the stitching method can be a valuable approach, if properly applied, to improve the quality of the XCT experimental results. All the results obtained with a reasonably strong signal gave an average result within a margin of 4% of the nominal depth.

Two important and common factors for all procedure stages seem to be taken into account before attempting modification, namely, zero-padding and windowing. The latter changes the contributions from different parts of the spectrum and thus eliminates many of the artifacts and "ghost" features, but also causes an additional shift in the peak position in some cases described

above. As the window filter multiplies the spectrum directly before the transformation, it requires deconvolution of the transformation result. The zero-padding step, even if it does not change the resolution, can correct some small shifts of the peaks resulting from too low sampling rate, but one has to be careful in case of extended low-signal spectral parts, as they can be treated as non-zero-padding in the subsequent processing.

The discrepancy between the results obtained with different source filtering is a serious problem, since it reached in our case up to 10% of the nominal value. The presence of the effect under idealized conditions of the model suggests that the experimental work was correct, and the reason for the effect is of a more general physical nature. We tend to ascribe the main responsibility for this behavior to the phenomena occurring at the spectral area adjacent to the silicon *L*-absorption edge. These phenomena include ionization and radiation emission in both silicon and gold. Silicon tends towards metallization and the effects at the contact surface of both materials, *e.g.*, plasmons can noticeably modify the phase of the propagating radiation. Moreover, the interfaces Si/Au and Au/Si seem to be very critical spots in the arrangement. Revealing the real reasons for the described discrepancy constitutes a very challenging task and, as we stressed earlier, it was out of the paper's scope.

Acknowledgements

The authors are thankful to Prof. Gerhard Paulus, Drs Silvio Fuchs, and Julius Reinhard from the University of Jena, Germany for helpful discussions on the project topic as well as to Dr Piotr Nyga from the Military University of Technology and Maciej Filipiak from the Centre for Advanced Materials and *Technologies* (CEZAMAT) both at Warsaw, for preparation of the nano-structured samples used in the experiment.

This work was supported by *National Science Center* (NCN) under grant No 2021/41/N/ST7/03198.

References

[1] Stöhr, J. (1992). NEXAFS Spectroscopy. In *Springer series in surface sciences*. Springer-Verlag Berlin, Heidelberg. https://doi.org/10.1007/978-3-662-02853-7

[2] Bunker, G. (2010). *Introduction to XAFS. A Practical Guide to X-Ray Absorption Fine Structure Spectroscopy*, Cambridge University Press, Cambridge. https://doi.org/10.1017/cbo9780511809194

[3] Maria, M., Anisimov, A. G., Stols-Witlox, M., & Groves, R. M. (2020). Spectra stitching for ultra-high resolution, low sensitivity decay and high-speed SD-OCT. In *Design and Quality for Biomedical Technologies XIII* (Vol. 11231, p. 3). SPIE. https://doi.org/10.1117/12.2545157

[4] Fuchs, S., Blinne, A., Rödel, C., Zastrau, U., Hilbert, V., Wünsche, M., Bierbach, J., Frumker, E., Förster, E., & Paulus, G. G. (2012). Optical coherence tomography using broad-bandwidth XUV and soft X-ray radiation. *Applied Physics B*, *106*(4), 789–795. https://doi.org/10.1007/s00340-012-4934-8

[5] Fuchs, S., Rödel, C., Blinne, A., Zastrau, U., Wünsche, M., Hilbert, V., Glaser, L., Viefhaus, J., Frumker, E., Corkum, P., Förster, E., & Paulus, G. G. (2016). Nanometer resolution optical coherence tomography using broad bandwidth XUV and soft X-ray radiation. *Scientific Reports*, *6*(1). https://doi.org/10.1038/srep20658

[6] Fuchs, S., Wünsche, M., Nathanael, J., Abel, J. J., Rödel, C., Biedermann, J., Reinhard, J., Hübner, U., & Paulus, G. G. (2017). Optical coherence tomography with nanoscale axial resolution using a laser-driven high-harmonic source. *Optica*, *4*(8), 903. https://doi.org/10.1364/optica.4.000903

[7] Wachulak, P., Bartnik, A., & Fiedorowicz, H. (2018). Optical coherence tomography (OCT) with 2 nm axial resolution using a compact laser plasma soft X-ray source. *Scientific Reports*, *8*(1). https://doi.org/10.1038/s41598-018-26909-0

[8] Huang, D., Swanson, E. A., Lin, C. P., Schuman, J. S., Stinson, W. G., Chang, W., Hee, M. R., Flotte, T., Gregory, K., Puliafito, C. A., & Fujimoto, J. G. (1991). Optical coherence tomography. *Science*, *254*(5035), 1178–1181. https://doi.org/10.1126/science.1957169

[9] Fercher, A. F., Drexler, W., Hitzenberger, C. K., & Lasser, T. (2003). Optical coherence tomography - principles and applications. *Reports on Progress in Physics*, *66*(2), 239–303. https://doi.org/10.1088/0034-4885/66/2/204

[10] Wang, R. K. (1999). Resolution improved optical coherence-gated tomography for imaging through biological tissues. *Journal of Modern Optics*, *46*(13), 1905–1912. https://doi.org/10.1080/09500349908231380

[11] Kulkarni, M., Thomas, C., & Izatt, J. (1997). Image enhancement in optical coherence tomography using deconvolution. *Electronics Letters*, *33*(16), 1365–1367. https://doi.org/10.1049/el:19970913

[12] Izatt, J. A., Choma, M. A., & Dhalla, A. (2015). Theory of Optical Coherence Tomography. In *Optical Coherence Tomography* (pp. 65–94). Springer, Cham. https://doi.org/10.1007/978-3-319-06419-2_3

[13] Hee, H. R. *et al.* (2002). Optical coherence tomography: Theory. In Bouma, B. E. and Tearney, G. J. (Eds.), *Handbook of Optical Coherence Tomography*. Taylor & Francis and CRC Press, Boca Raton, 2001. https://doi.org/10.1201/9780367800819

[14] Wolf, E. (1996). Principles and development of diffraction tomography. In Consortini, A. (Ed.) *Trends in Optics.* (pp. 83–110). Academic Press. https://doi.org/10.1016/B978-012186030-1/50007-2

[15] Gastinger, K. (2008). Low coherence speckle interferometry (LCSI): when speckle interferometry goes sub-surface In *Proceedings of Eighth International Conference on Correlation Optics*, 70081I – 10. https://doi.org/10.1117/12.797354

[16] Bouma, B. E. and Tearney, G. J. (2002). Optical source. In Bouma, B. E. and Tearney, G. J. (Eds.), *Handbook of Optical Coherence Tomography*, Taylor & Francis and CRC Press, Boca Raton, 2001. https://doi.org/10.1201/9780367800819

[17] Voelz, D. (2011). *Computational Fourier Optics: a MATLAB Tutorial.* Tutorial Texts, SPIE Press, Bellingham, Washington USA. https://doi.org/10.1117/3.858456

[18] Goodman, J. W. (1996). *Introduction to Fourier Optics.* 2nd Edition, McGraw Hill Series in Electrical and Computer Engineering. Electromagnetics, The McGraw Hill, New York.

[19] Ersoy, O. K. (2007). *Diffraction, Fourier Optics and Imaging.* Wiley Interscience, John Wiley & Sons Inc., Hoboken, New Jersey.

[20] Center for X-Ray Optics (n.d.) *CXRO X-Ray Interactions With Matter*, https://henke.lbl.gov/optical_constants/

[21] Born, M., & Wolf, E. (1999). *Principles of optics*. 7th Edition. Cambridge University Press. https://doi.org/10.1017/cbo9781139644181

[22] Shekhar, P., Pendharker, S., Sahasrabudhe, H., Vick, D., Malac, M., Rahman, R., & Jacob, Z. (2018). Extreme ultraviolet plasmonics and Cherenkov radiation in silicon. *Optica*, *5*(12), 1590. https://doi.org/10.1364/optica.5.001590

[23] Strickland, D. J. & Lin, D. L. (1979). *Soft X-ray photoemission properties for newly modeled materials gold, silver,copper, and carbon.* Final Report DNA 001-77-C-0209 for Defence Nuclear Agency

[24] Hummel, R. E. (2003). *Electronic Properties of Materials*. 3rd Edition, Springer Science + Business Media Inc., New York. https://doi.org/10.1007/978-1-4419-8164-6

[25] Lässer, R., & Smith, N. (1981). Interband optical transitions in gold in the photon energy range 2–25 eV. *Solid State Communications*, *37*(6), 507–509. https://doi.org/10.1016/0038-1098(81)90488-9

[26] Haruyama, Y., Kanda, K., & Matsui, S. (2004). Study of Au–Si(100) interface by means of Si 2p core-level photoemission spectroscopy. *Journal of Electron Spectroscopy and Related Phenomena*, *137–140*, 97–100. https://doi.org/10.1016/j.elspec.2004.02.031

[27] Franciosi, A., Niles, D. W., Margaritondo, G., Quaresima, C., Capozi, M., & Perfetti, P. (1985). Au-Si interface formation: The other side of the problem. *Physical Review. B, Condensed Matter*, *32*(10), 6917–6919. https://doi.org/10.1103/physrevb.32.6917

[28] Perfetti, P., Nannarone, S., Patella, F., Quaresima, C., Capozi, M., Savoia, A., & Ottaviani, G. (1982). Low-energy electron-loss spectroscopy and Auger-electron-spectroscopy studies of noble-metal—silicon interfaces: Si-Au system. *Physical Review. B, Condensed Matter*, *26*(3), 1125–1138. https://doi.org/10.1103/physrevb.26.1125

[29] Arikkatt, A. J., Węgrzyński, Ł., Bartnik, A., Fiedorowicz, H., & Wachulak, P. (2022). Laboratory system for optical coherence tomography (OCT) using a laser plasma source of soft x-rays and extreme ultraviolet and focusing ellipsoidal optics. *Optics Express*, *30*(8), 13491. https://doi.org/10.1364/oe.454656

Antony Jose Arikkatt received his M.Sc degree in optical engineering from Warsaw University of Technology (WUT), Poland in 2018. He is pursuing his Ph.D degree in X-ray coherence tomography in Military University of Technology (WAT), Warsaw, Poland. He is currently working with ASML, Netherlands, as optical sensing engineer. His main interests are in X-ray optics, laser plasma, plasma physics, fiber optics and holography.

Andrzej Bartnik received his Ph.D. Degree from Military University of Technology, Warsaw, Poland, in 1996, in material engineering and D.Sc. degree from Military University of Technology, in 2016 in electronics. Currently holds position of an associate professor at the Institute of Optoelectronics, MUT, Warsaw, Poland. His main interests are development of laser-produced plasma soft X-ray and extreme ultraviolet sources, research concerning interaction of high intensity ionizing radiation with matter, micromachining and surface modification of solids, creation and investigation of photoionized plasmas.

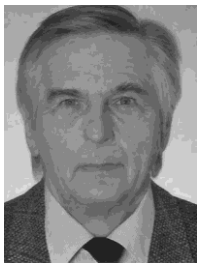

Karol A. Janulewicz obtained his Ph. D. degree in quantum electronics in 1990 from the Warsaw University of Technology, Warsaw (Poland) and habilitation degree (D. Sc.) in 2018 from the Military University of *Technology* (MUT) in Warsaw. Recently, he was with MUT as a universi-ty professor. His scientific interests concentrate on laser physics, laser-matter interaction both focused on the X-ray spectral range and plasma physics. He is also interested in ultra-fast processes initiated by radiation, X-ray spectroscopy and plasmonics.

Przemyslaw W. Wachulak obtained his Ph. D. degree in Electrical and Computer Engineering, major: extreme ultraviolet technology, from the Colorado State University (CSU), Fort Collins, Colorado, USA in 2008, habilitation degree (D. Sc.) in physics in 2013 from the University of Warsaw, and Full Professorship in 2018. Currently, he holds the position of full professor and rector of the Military University of Technology, Warsaw, Poland. His work focuses on the development of new laser-plasma sources for the generation of extreme ultraviolet and soft X-ray radiation for applications in nanoimaging, holography, absorption spectroscopy, optical coherence tomography, metrology, and radiobiology.

Henryk Fiedorowicz earned a master's degree in nuclear physics in 1975 and a doctorate in plasma physics in 1989, both from the Military University of Technology. After graduating, he joined the Institute of Plasma Physics and Laser Microfusion in Warsaw to study laser-generated plasmas and laser-driven nuclear fusion using X-ray diagnostics. In 1992, he joined the Institute of Optoelectronics of the Military University of Technology, where he established the Laser-Matter Interaction Laboratory (LMI Lab). From 2002 to 2010, he served as director of the Institute of Optoelectronics. He is currently a professor at the Military University of Technology. His primary research and development work focuses on laser-plasma sources of X-ray and extreme ultraviolet radiation for applications in various fields of science and technology.